

Review

On Metal Segregation of Bimetallic Nanocatalysts Prepared by a One-Pot Method in Microemulsions

Concha Tojo ^{1,*}, David Buceta ² and Manuel Arturo López-Quintela ²

¹ Physical Chemistry Department, University of Vigo, E-36310 Vigo, Spain

² Laboratorio de Magnetismo y Nanotecnología, University of Santiago de Compostela, E-15782 Santiago de Compostela, Spain; buceta.david@gmail.com (D.B.); a.lopez@nanogap.es (M.A.L.-Q.)

* Correspondence: ctojo@uvigo.es; Tel.: +34-986812299

Academic Editors: Alain Roucoux and Audrey Denicourt

Received: 28 December 2016; Accepted: 10 February 2017; Published: 17 February 2017

Abstract: A comparative study on different bimetallic nanocatalysts prepared from microemulsions using a one-pot method has been carried out. The analysis of experimental observations, complemented by simulation studies, provides detailed insight into the factors affecting nanoparticle architecture: (1) The metal segregation in a bimetallic nanocatalysts is the result of the combination of three main kinetic parameters: the reduction rate of metal precursors (related to reduction standard potentials), the material intermicellar exchange rate (determined by microemulsion composition), and the metal precursors concentration; (2) A minimum difference between the reduction standard potentials of the two metals of 0.20 V is needed to obtain a core-shell structure. For values $\Delta\epsilon^0$ smaller than 0.20 V the obtaining of alloys cannot be avoided, neither by changing the microemulsion nor by increasing metal concentration; (3) As a rule, the higher the film flexibility around the micelles, the higher the degree of mixture in the nanocatalyst; (4) A minimum concentration of metal precursors is required to get a core-shell structure. This minimum concentration depends on the microemulsion flexibility and on the difference in reduction rates.

Keywords: bimetallic nanoparticles; nanocatalysts; microemulsion; simulation; one-pot method

1. Introduction

Obtaining nanoparticles is currently a very active research field with a wide variety of technical applications in catalysis [1–3], photonics [4], and energy conversion and storage devices [5–7]. The applications of nanoparticles are expected to improve many fields of advanced materials.

1.1. Bimetallic Nanoparticles as Catalysts

One of the fundamental attractions of metallic nanoparticles is the improvement of catalysts [8,9] due to the obvious increase in the active surface area compared with existing metal particles. As an example, a reduction in Pt content of the Pt-based catalysts would be very interesting in the automotive industry. In this line, a great effort lies on improving Pt catalysts. One option is using Pt alloys instead of pure Pt in the catalyst. From the pioneering contribution of Sinfelt [10,11], the interest in developing new catalysts composed by two metal components have been paid special attention. The presence of a second metal in a bimetallic nanoparticle not only reduces the cost as some noble metal that is substituted by a non-noble one, but also modifies the interactions between atoms giving rise to changes in the structure and surface. The electron interactions between two metal atoms, which are electron-rich, just as the heterometallic bonding interactions change the surface electronic properties of the nanoparticles [12–19]. As a rule, the catalytic behaviour is usually enhanced on bimetallic nanoparticles as compared to monometallic nanoparticles [3,7,13–15,17–21] even at low

temperatures [22,23]. This can be attributed to the presence of a second metal, which changes both geometrical and electronic properties due to the electronic coupling between the individual metals. The overall efficiency observed in bimetallic nanocatalysts accounts for synergistic effects between the two metals [20,24,25]. The synergetic catalytic effect was defined by Shi [26] as “a certain kind of cooperation between different components and/or active sites in one catalyst, which results in significantly, or even strikingly, enhanced catalytic performances than the arithmetic summation of those by corresponding individual components”. As an example, the catalysis of CO oxidation is improved by Au-Ag nanocatalysts because of the synergistic interaction between the two metals. In this case study, Ag adsorbs reactive oxygen species and Au adsorbs CO [25]. The progress in this field has been extremely important, and currently a number of bimetallic catalysts are widely utilized in different kinds of reactions [2], such as hydrogenation [27–30], reforming reactions [31,32], oxidation [25,33–37], oxygen reduction reactions [1,14,22,38–41], hydrogenolysis [10,42,43] and coupling reactions [20,44–46]. Moreover, it is important to point out that bimetallic nanocatalysts were proposed as candidates in green chemistry and future biomass-based refineries [42,47]. Another advantage of the bimetallic nanoparticles as catalysts is a superior longevity of the bimetallic catalyst compared with a monometallic one. For example, in the dehydrogenation reaction of formic acid catalyzed by Au-Pd bimetallic nanoparticles, the presence of Au inhibits the poisoning of the active sites of Pd by CO (produced in a secondary reaction) [7]. In general, the catalyst stability can be improved by the presence of the second metal, which allows its recovery and recycling [46]. Finally, bimetallic catalysts show well-defined active sites within the nanoparticle, contrary to the mixed and unspecified active sites in bulk heterogeneous catalysts [20]. Excellent review articles including the role of bimetallic nanoparticles as catalysts are already available [2,3,20,48–51].

1.2. Metal Arrangement in Bimetallic Nanoparticles

Controlling the arrangement of the two metals within the first atomic layers from the surface of the bimetallic nanoparticle is essential to improve the catalytic activity [2,52–55]. It is important to note that the synergistic effect exhibited by bimetallic nanocatalysts is strongly dependent on the surface composition [55]. It is well known that heterogeneous catalytic reactions take place on the surface of catalysts, where the adsorption and desorption of the reactants, intermediates and products occur. The synergic cooperation between both metals modifies the surface electronic properties, so the improvement of catalysis is conditioned by the ability to control the surface composition. Hence, different Au-Pt nanostructures are used as catalysts depending on the metal distribution: for electro-oxidation of methanol, the preferred structure is a Pt-Au alloyed shell [37]. Conversely, an Au-core/Pt-shell nanoparticle is better to catalyze oxygen reduction reaction [38,56], or formic acid electro-oxidation [57]. For this reason, the surface composition of bimetallic nanocatalysts is a critical aspect to take into account.

According to the mixing pattern, bimetallic nanoparticles can be classified as core-shell, subcluster segregated or nanoalloy [3,58]. The first one consists of a core composed by one of the metals, which is covered by a shell of another, including some mixing between both of them. In fact, using noble metals as shell materials in a core-shell nanoparticle offers economic advantages because it maximizes the noble element surface to volume ratio. Furthermore, when magnetic elements (such as Fe, Co, and Ni) are used as a core metal, the noble shells' nanoparticles may acquire magnetic properties [59]. The second type of bimetallic arrangement consists of two clearly separated metals, not surrounding one another, but adjacent to each other. It is a segregated subcluster. Finally, nanoalloys, either crystalline ordered or random, are composed of mixed architectures of the two metals. Magno et al. [60] pay attention so as to distinguish between intermetallic structures and alloys. In an intermetallic arrangement, the mixtures of metals shows a specific lattice structure, that is, different from those of its constituent metals. On the contrary, in an alloy the lattice structure is the same as that of its main compound.

Rai et al. [46] suggest that the synergic cooperation between the two metals is more noticeable in alloyed nanoparticles, due to the higher probability of metal-metal interactions in comparison to core-shell ones.

1.3. Synthesis of Bimetallic Nanoparticles in Microemulsions

Since the control of metal distribution in a bimetal nanostructure is crucial to the enhancement of catalysts performance, many efforts are being devoted to study innovative techniques to obtain different bimetallic nanostructures, including multistep synthesis [61], electrochemical dealloying [6,39–41], impregnation [7,48], chemical reduction [49,50], thermal decomposition [62], electrochemical synthesis [3,63,64], microwave synthesis [65,66] and synthesis in microemulsions [30], as summarized in various reviews [2,50,51].

One of the most common procedures is the chemical reduction of the two metal ions using a one-pot synthesis. The difference in reduction kinetics of both metal ions results in the formation of the faster reduction metal, which becomes the seed for the subsequent deposition of another metal, which builds up the surrounding shell. In the case of almost similar reduction rates, a mixed nanoalloy is obtained. That is, the reduction potentials, i.e., the tendency of the salt to become reduced, are expected to be determinants for the final arrangement [67]. Irrespective of the synthesis route, the ideal technique must ensure controllability of the nanostructure, which turns out to be hardly achieved. Specifically, controlling the metal distribution in the nanoparticle surface when a one-pot method is used remains a challenge [22,23,52,68–70].

Due to the enormous volume of work in bimetallic nanoparticle preparation, in the current review we will focus on the synthesis of nanoparticles in microemulsions. The microemulsion route is one of the most preferred candidates to control the size and composition of bimetallic nanoparticles. In this method, small quantities of water are added to a solution of surfactant/oil. The resulting mixture can form reverse micelles (nanometer-sized water droplets dispersed in the oil phase) stabilized by a surfactant film. When the metal precursors are solved inside the water droplets, the addition of a reducing agent (solved in another similar microemulsion) can result in the formation of monodispersed metal particles inside these aqueous nanoreactors. The key aspect is that the nucleation and growth of the particles take place within the confined space of inversed micelles. In this way, the surfactant molecules prevent particles from agglomeration and, hence, make possible high yield and monodispersity. The exchange of the reacting species between micelles is believed to occur by direct transfer between micelles during their collision [71]. One of the main advantages of this method is that nanoparticle size can be directly controlled by the water/surfactant ratio. Another advantage of the microemulsion route is that nanoparticles can be synthesized at room temperature, and surfactants around the particles can be removed with ease. However, even with this method, the final arrangement seems to depend on many factors, such as the mixing pattern of reactants, the pair of metals, specific precursors, the microemulsion composition, concentration, etc.

1.4. Scope

It would be a great improvement if the nanostructure could be tuned a priori by selecting the most suitable synthetic conditions. In this way, a catalyst would not only be characterized once the synthesis is completed, but also designed and synthesized with specific composition and nanoarchitecture for a particular reaction of interest. To achieve this aim, a systematic study taking all of the experiments together is strongly needed. In this paper we pool the results from all 32 studies and reanalyse them together to determine if, and in what conditions, common criteria can be taken over or generalised. It would not only allow avoiding unwanted structures, but also relate the synthesis variables with the final nanoarchitecture of the particles. Since many factors control the final metal arrangement in the bimetallic nanoparticle, an enormous trial-and-error effort would be required to achieve such a challenging objective. Hence, we developed a Monte Carlo simulation to predict the nanostructure in terms of type of microemulsion and metals employed [72]. In this contribution, we are focused

on the one pot method in microemulsions. In doing so, rather than making an extensive review of all work carried out in the field, only those studies that meet the requirements, that is, nanoparticles synthesized in microemulsions using a one-pot method, have been included.

In this review we highlighted recent findings concerning the factors that govern the metal arrangement of bimetallic nanoparticles synthesized in microemulsions. In Section 2 the experimental observations taken from different authors are described. In Section 3, the resulting metal arrangement of different bimetallic structures under different reactions conditions are discussed in light of the Monte Carlo simulation results. In the final section the main conclusions and recommendations for further advancing bimetallic nanoparticle synthesis are pointed out.

2. Bimetallic Nanoparticles Obtained from Microemulsions Using a One Pot Method. Experimental Observations

Different bimetallic nanoparticles have been obtained by microemulsion route. In order to compare results, we will focus on the exact same synthetic method: first, each reactant (both metal salts and reducing agent) is solved inside a microemulsion, then microemulsions are mixed, so micelles move and collide with each other, allowing the exchange of material. The reduction takes place when one metal salt and the reducing agent are located inside the same micelle. Eventually nanoparticles are built up by the aggregation of resulting metallic atoms in the water phase. This pattern of reactants mix, called a one-pot method, allows the simultaneous reduction of the two metals, in contrast to a post-core method.

Table 1 shows results taken from the literature, restricted to bimetallic nanoparticles obtained with a one-pot method in microemulsions. Table 1 includes the difference in the standard reduction potential of the two metals, the structure of the resulting nanoparticle, and information about the microemulsion composition, metal precursors, reduction agent, surfactant film flexibility, metal ions concentration (based on the volume of aqueous solution in the reverse micelles; molar ratio 1:1) and final nanoparticle size, if available. The criterion to arrange results in Table 1 was the difference in standard reduction potential for each pair of metals. The reason is that, a priori, reduction of the two metals may take place simultaneously, but it is well-known that the higher reduction potential ions have the priority in reduction. As a consequence, it is expected that a large difference in the reduction potentials will lead to a core-shell structure, and a small difference results in a nanoalloy [67]. However one has to be careful when applying bulk ideas to compartmentalized media [73] because nanoparticle structure not only depends on the difference in reduction rates, but also on the microemulsion composition [72,74], reactant concentrations [75], and the proportion between reactants [75,76]. Therefore, the experiments collected in Table 1 will be discussed in light of the different factors affecting metal arrangement.

Ag-Pt nanoparticles were obtained in a water/dioctyl sodium sulfosuccinate (AOT)/isooctane microemulsion ($\omega = [\text{H}_2\text{O}]/[\text{AOT}] = 6$) by simultaneous reduction of H_2PtCl_6 and AgNO_3 with hydrazine [77]. The nanoparticle size was determined by transmission electron microscopy (TEM). The size was 4.2 ± 0.9 nm for a bimetallic nanoparticle Pt-Ag (1:1) and using a metal salts concentration 0.1 M. Energy dispersive X-ray (EDX) and X-ray photoelectronic spectroscopy (XPS) measurements indicate that nanoparticles show a homogeneous alloy structure. According to XPS data, the mole fraction of Pt in the nanoparticle surface has a linear relationship with the mole fraction of Pt in the feeding solution. Due to the reduction potential of Ag^+ ions ($\epsilon^0 = 0.80$ V) is insignificantly higher than that of PtCl_6^{2-} ($\epsilon^0 = 0.74$ V), the difference in redox potentials is almost irrelevant ($\Delta\epsilon^0 = 0.06$ V), resulting in a simultaneous reduction of both metals, which justifies the homogeneous alloy structure.

A slightly higher difference in reduction potentials is shown by Pd-Ag nanoparticles, which were prepared at various Pd/Ag atomic ratios in a water/Brij30/n-octane microemulsion [78]. Samples were characterized by ultraviolet-visible (UV-VIS), high-resolution transmission electron microscopy (HRTEM), EDX, X-ray diffraction (XRD), and XPS. The analyses indicate the formation of bimetallic alloy nanoparticles with a face-centred cubic (fcc) structure. A high activity and selectivity for selective hydrogenation of acetylene was achieved. In another experiment, Pd-Ag nanoparticles were prepared

from a water/AOT/isooctane microemulsion, and they also did not show metal segregation [19]. Pd-Ag nanoparticles also showed catalytic activity in the Heck reaction, even though Pd-Cu and Pd-Ni proved to be better catalysts with higher activity and selectivity.

Pt-Ru nanocatalysts ($\Delta\varepsilon^0 = 0.14$ V) have been prepared under different synthetic conditions (different microemulsion compositions and reactant concentrations) [79–83]. An exhaustive characterization of the samples (XPS, X-ray diffraction, TEM) proved the presence of Pt-Ru alloys with an fcc structure in all cases. Only XPS measurements in [82] suggest a slightly Ru-enriched surface. Pt-Ru nanoparticles of different Pt-Ru composition showed catalytic activity in CO adsorption-oxidation and electrochemical oxidation of methanol [79–81].

Pt-Pd nanoparticles ($\Delta\varepsilon^0 = 0.15$ V) at various molar ratios have been prepared by co-reduction with hydrazine in different microemulsions [84–86]. The resultant nanoparticles were characterized by TEM, XRD, EDX, and XPS. The nanoparticles had a homogeneous alloy structure at molar ratio 1:1, and only an enrichment of Pt on particle surface was observed at a 9:1 molar ratio Pd-Pt [84]. Yashima et al. [86] studied the catalytic activity for CO oxidation. The highest catalytic activity was shown by a 20:80 Pt:Pd molar ratio, contrary to the behaviour observed in conventional wet-impregnated Pt-Pd catalysts, which showed the highest catalytic activity with a 50:50 molar ratio.

An incipient metal segregation in Au-Ag nanoparticles ($\Delta\varepsilon^0 = 0.20$ V) was observed by Chen et al. [87]. UV-VIS, XRD, and HRTEM experiments revealed the formation of Au-Ag bimetallic nanoparticles, and the EDX analysis showed that outer layers were enriched in Ag atoms. The formation rate of Au nanoparticles was proved to be much quicker than that of Ag. It was proposed that Au might act as the seeds for the formation of Au-Ag bimetallic nanoparticles. However, true homogeneous alloys, not of a core-shell type, were obtained under different synthesis conditions (higher film flexibility and smaller reactants concentration) [88,89]. The formation of Au-Ag in alloy form rather than a mixture of individual particles was attributed to very similar lattice constants (0.408 and 0.409 nm for gold and silver respectively) [89].

Fe-Ni nanoparticles ($\Delta\varepsilon^0 = 0.20$ V) were obtained from microemulsions as an alloy in a 20:80 Fe:Ni molar ratio [74]. Alloyed nanoparticles exhibit a primitive cubic (pc) structure, different from the body-centred cubic (bcc) structure of the bulk material. Furthermore, the dependence of the nanoparticle morphology on the microemulsion composition (water to surfactant ratio) was also stated. It was observed that nanoparticle magnetization was much lower than the bulk material.

A different degree of metal separation was obtained for Au-Pt nanoparticles ($\Delta\varepsilon^0 = 0.26$ V) synthesized under different reaction conditions. On the one hand, nanoparticles showed core-shell structures when the microemulsion was prepared using rigid surfactants such as AOT [90] and Brij-30 [91]. On the other hand, more flexible surfactants (Tergitol [22] and TritonX-100 [92]) lead to alloyed nanoparticles. Moreover, a metal separation dependent on reactant concentration and reactants' molar ratios was established both experimentally and by simulation [75]. The activity of Au-Pt nanoalloys as electrocatalysts for the oxygen reduction reaction was proved to be better than that of the Au-Pt segregated particles [22].

The metal separation in Au-Pd nanoparticles ($\Delta\varepsilon^0 = 0.39$ V) was also dependent on microemulsion composition, as shown in Table 1. According to the XPS study, the outer part of Au-Pd particle prepared in a water/AOT/isooctane microemulsion is enriched in Pd, suggesting a core-shell structure [93]. A palladium-rich surface was also obtained when Brij-30 was used as a surfactant [94]. The resulting particles showed an optimum performance as electrocatalysts toward the borohydride oxidation reaction (up to 50% of Pd can be substituted by Au without diminishing the catalytic activity of monometallic Pd) [94]. On the contrary, homogeneous Au-Pd nanoalloys were prepared in a water/TritonX-100/n-hexane/n-hexanol microemulsion [95]. Cyclic voltammetric and chronoamperometric measurements were used to investigate the catalytic performance, and it showed that Au-Pd nanocatalysts exhibit higher electrocatalytic activity for ethanol oxidation and better tolerance to poisoning than pure Pd nanoparticles and bimetal nanoparticles prepared in an aqueous solution.

Table 1. Bimetallic nanoparticles obtained by a one-pot method in microemulsions.

N°	Metals	$\Delta\epsilon^0/V$	Structure	Microemulsion; Reduction Agent; Metal Precursor	Film Flex	c/M	Size/nm	Ref.
1	Ag-Pt	0.06	alloy	water/AOT/isooctane; N ₂ H ₅ OH; Ag ⁺ , PtCl ₆ ²⁻	rigid	0.1	4.2	[77]
2	Pd-Ag	0.12	alloy	water/Brij30/n-octane; N ₂ H ₄ ; Ag ⁺ , Pd ²⁺	rigid	-	2	[78]
3			alloy	water/AOT/isooctane; N ₂ H ₄ ; Ag ⁺ , Pd ²⁺	rigid	-	-	[19]
4	Pt-Ru	0.14	alloy	water/Brij-30/n-heptane; NaBH ₄ ; PtCl ₆ ²⁻ , Ru ³⁺	rigid	0.1	3.7	[79]
5			alloy	water/Berol 050/isooctane; N ₂ H ₅ OH; PtCl ₆ ²⁻ , Ru ³⁺	flex	-	-	[80]
6			alloy	water/NP5-NP9/cyclohexane; NaBH ₄ ; PtCl ₆ ²⁻ , Ru ³⁺	flex	0.025	4–9	[81]
7			alloy	water/igepal CA-630/isooctane/2-propanol; NaBH ₄ ; PtCl ₆ ²⁻ , Ru ³⁺	flex	0.004	2–4	[82]
8			alloy	water/TritonX-100/propanol/cyclohexane; NaBH ₄ ; PtCl ₆ ²⁻ , Ru ³⁺	flex	0.002	2.5–4.5	[83]
9	Pt-Pd	0.15	alloy	water/AOT/isooctane; N ₂ H ₅ OH; PdCl ₄ ²⁻ , PtCl ₆ ²⁻	rigid	0.1	9.8	[84]
10			alloy	water/C ₁₂ E ₅ /hexadecane; N ₂ H ₅ OH; Pd ²⁺ , PtCl ₆ ²⁻	flex	-	-	[85]
11			alloy	water/Brij-L4/cyclohexane; N ₂ H ₅ OH; Pd ²⁺ , Pt ²⁺	rigid	-	-	[86]
12	Au-Ag	0.20	Au core-enriched in Ag shell	water/AOT/isooctane; N ₂ H ₅ OH; Ag ⁺ , AuCl ₄ ⁻	rigid	0.1	5.1	[87]
13			alloy	water/C ₁₁ E ₃ -C ₁₁ E ₅ /cyclohexane; NaBH ₄ ; Ag ⁺ , AuCl ₄ ⁻	flex	0.05	6.7	[88]
14			alloy	water/TritonX-100/cyclohexane NaBH ₄ ; Ag ⁺ , AuCl ₄ ⁻	flex	0.05	23	[89]
15	Fe-Ni	0.20	alloy	water/CTAB/isooctane/n-butanol; NaBH ₄ ; Fe ²⁺ , Ni ²⁺	very flex	0.4/0.1	4–12	[74]
16	Au-Pt	0.26	core-shell	water/AOT/isooctane; N ₂ H ₅ OH; AuCl ₄ ⁻ , PtCl ₆ ²⁻	rigid	0.5	3.8	[90]
17			alloy/Pt enriched surface	water/Brij 30/n-heptane; NaBH ₄ ; AuCl ₄ ⁻ , PtCl ₆ ²⁻	rigid	-	-	[91]
18			core-shell	water/tergitol/isooctane; N ₂ H ₅ OH; AuCl ₄ ⁻ , PtCl ₆ ²⁻	flex	0.08–0.4	-	[75]
19			alloy	water/tergitol 15-S-5/isooctane; N ₂ H ₅ OH; AuCl ₄ ⁻ , PtCl ₆ ²⁻	flex	-	-	[22]
20			alloy	water/TritonX-100/cyclohexane/1-hexanol; NaBH ₄ ; AuCl ₄ ⁻ , PtCl ₆ ²⁻	flex	2.7 × 10 ⁻⁴	2.5	[92]
21	Au-Pd	0.39	core-shell	water/AOT/isooctane; N ₂ H ₅ OH; AuCl ₄ ⁻ , PdCl ₄ ²⁻	rigid	0.5	2.8	[93]
22			enriched in Au core/enriched in Pd shell	water/Brij-30/n-heptane; NaBH ₄ ; AuCl ₄ ⁻ , PdCl ₄ ²⁻	rigid	-	5.0	[94]
23			alloy	water/TritonX-100/n-hexane/n-hexanol; N ₂ H ₅ OH; AuCl ₄ ⁻ , PdCl ₆ ⁴⁻	flex	0.005/0.006	5.1	[95]
24	Pt-Cu	0.40	alloy	water/AOT/hexane; N ₂ H ₅ OH; Cu ²⁺ , PtCl ₆ ²⁻	rigid	0.058/0.015	3	[16]
25			PtCu ₃ alloy	water/CTAB/isooctane/n-butanol; N ₂ H ₅ OH; Cu ²⁺ , PtCl ₆ ²⁻	very flex	0.02	1.6	[96]
26	Pt-Bi	0.43	PtBi ₂ intermetall	water/Brij-30/n-octane/1-octanol; NaBH ₄ ; Bi ³⁺ , PtCl ₆ ²⁻	rigid	0.013	4.5	[60]
27	Cu-Ni	0.59	alloy	water/SDS/n-butanol/n-heptane; N ₂ H ₅ OH; Cu ²⁺ , Ni ²⁺	very flex	-	4.6–9.3	[67]
28			alloy	water/CTAB/isooctane/1-butanol; N ₂ H ₅ OH; Cu ²⁺ , Ni ²⁺	very flex	0.1	7	[76]
29	Pt-Pb	0.87	intermetal (Pt/Pb ₃ , Pt/Pb)	water/Brij-30/n-octane/1-octanol; NaBH ₄ ; Pb ²⁺ , PtCl ₆ ²⁻	rigid	0.013	4.0	[60]
30	Pt-Co	1.02	alloy	water/TritonX-100/cyclohexane/propanol; NaBH ₄ ; PtCl ₆ ²⁻ , Co ²⁺	flex	0.04/0.120	3–4	[97]
31	Ag-Ni	1.04	core-shell	water/OP-4,OP-7/n-heptane; NaBH ₄ ; Ag ⁺ , Ni ²⁺	flex	-	50–100	[98]
32	Pd-Ni	1.15	alloy	water/AOT/isooctane; N ₂ H ₅ OH; Pd ²⁺ , Ni ²⁺	rigid	0.0017	6–20	[99]

XRD measurements proved the crystalline nature of Pt-Cu ($\Delta\varepsilon^0 = 0.40$ V) alloyed nanocatalysts prepared via microemulsion [16]. These Pt-Cu nanoparticles were utilized as catalysts for the reduction of dye rodhamine B. Catalytic performance confirmed that bimetalization improves the catalytic behaviour of Pt-Cu particles as compared to the individual monometallic nanoparticles. Pt-Cu nanoparticles were also prepared by Weihua et al. [96]. In this case, the synthesis was carried out in a very flexible microemulsion (water/cetyltrimethylammonium bromide (CTAB)/isooctane/n-butanol). Nanoparticles were characterized by HRTEM, XRD, and XPS measurements, which revealed the formation of PtCu₃ alloyed nanoparticles.

Magno et al. [60] synthesized Pt-Bi ($\Delta\varepsilon^0 = 0.43$ V) and Pt-Pb ($\Delta\varepsilon^0 = 0.87$ V) nanoparticles. In the case of Pt-Bi, EDX analysis showed two different regions, pure Pt and pure Bi, at a low reduction agent concentration. When the reduction agent was in excess, and under N₂ atmosphere in order to prevent metal oxidation by O₂, a single and ordered Pt-Bi intermetallic phase was obtained. Finally, if the reduction agent was added as a power (instead of mixing the microemulsions) intermetallic Pt-Bi₂ was formed. In the case of Pt-Pb, HRTEM and selected area electron diffraction (SAED) showed the presence of various intermetallic phases, namely Pt₃-Pb, Pt-Pb, and no experimental evidence of a core-shell structure.

Homogeneously-alloyed Cu-Ni ($\Delta\varepsilon^0 = 0.59$ V) particles were obtained from a water/SDS/n-butanol/n-heptane microemulsion [67]. The TEM, XRD, and EDX results provided evidence for the presence of a well-mixed Cu-Ni alloy. The composition and size of the alloyed particles were dependent on the water to surfactant mole ratio, the Cu:Ni mole ratio and the method of addition of metal precursors. It is of particular interest to note the change in nanostructure increasing ω ($\omega = [\text{water}]/[\text{surfactant}]$) and keeping the amount of total metal ions constant. At $\omega \geq 40$ (that is, large droplet size) Cu Ni nanocomposites were obtained rather than Cu-Ni alloys (prepared at $\omega \leq 32$). Authors suggested that this result is related to the large difference between reduction potentials of Cu and Ni. Alloyed Cu-Ni nanoparticles with different Cu:Ni ratios were also prepared by Ahmed et al. [76] using CTAB as a surfactant. A Ni enrichment in the shell is suggested from the depth profile curve from XPS studies at a 1:1 Cu:Ni ratio. A more homogeneous structure was deduced at 1:3 and 3:1 Cu:Ni ratios. These bimetallic nanoparticles showed ferromagnetic behaviour.

Pt-Co ($\Delta\varepsilon^0 = 1.02$ V) nanoalloys were also obtained from microemulsion [97]. The resulting particles were weakly crystalline, and no evidence of core-shell structure was reported. Like other bimetallic nanoparticles, Pt-Co exhibited a higher catalytic activity toward methanol oxidation than pure Pt nanoparticles.

Core-shell Ag-Ni ($\Delta\varepsilon^0 = 1.04$ V) nanoparticles were synthesized via microemulsion [98] using a molar ratio Ag:Ni 2:1. XRD measurements proved that both Ag cores and Ni shells show an fcc structure. The resulting nanocatalysts showed a high catalytic activity for degradation reaction of eosin Y.

Finally, Pd-Ni ($\Delta\varepsilon^0 = 1.15$ V) nanoparticles were prepared in a water/AOT/isooctane microemulsion with a 1:1 Pd:Ni ratio [99]. Although the main strengths of this research is the catalytic performances of Pd-Ni nanocatalysts for the C-N coupling reactions, XRD studies proved the formation of a true Pd-Ni alloy.

3. Factors Concerning Metal Separation in Bimetallic Nanoparticles

3.1. Keeping the Microemulsion Composition Fixed

At first sight, the sequence of the couple of metals according to the difference in reduction rates seems to offer a mixture of structures. The fact that a particular couple of metals can be obtained as alloy and core-shell architectures implies that the whole process is more complex than a competition between reduction rates. In consequence, in order to discriminate the influence of the reaction rates difference, only nanoparticles synthesized from the same microemulsion must be compared. A water/AOT/isooctane was used to prepare seven different bimetallic nanoparticles (see experiments

number 1, 3, 9, 12, 16, 21, 32. Keeping our attention on these experiences, it can be observed a clear tendency from nanoalloy (Ag-Pt [77], $\Delta\varepsilon^0 = 0.06$ V and Pt-Pd [84], $\Delta\varepsilon^0 = 0.15$ V) to a slightly segregated structure (Au core-enriched in Ag shell, Au-Ag [87], $\Delta\varepsilon^0 = 0.20$ V), to a clear segregated core-shell (Au-Pt [90], $\Delta\varepsilon^0 = 0.26$ V and Au-Pd [93], $\Delta\varepsilon^0 = 0.39$ V). That is, the larger the difference in reduction rates, the better the metal segregation, as expected. The only exception to this trend is the last experiment (Pd-Ni), which will be discussed later. The progressive metal segregation is also obtained using a water/Brij-30/n-heptane microemulsion (see experiments number 4, 17, 22): from nanoalloy (Pt-Ru [79], $\Delta\varepsilon^0 = 0.14$ V) to a Pt enriched surface (Au-Pt [91], $\Delta\varepsilon = 0.26$ V), to an enriched Au core/enriched Pd shell (Au-Pd [93], $\Delta\varepsilon^0 = 0.39$ V).

The better separation of the two metals as increasing the difference between reduction potentials can be clearly observed in the structures predicted by simulation [100]. Figure 1 shows simulation results on the distribution of the two metals (noted by A and B) forming the nanocatalyst, for different reduction rate ratios of the metals and maintaining a constant microemulsion composition (see Supporting Information for Simulation Details). When the reduction rates are equal (Figure 1a, $v_A/v_B = 1$) the composition of the inner layers (core) is variable: some particles are mainly composed of only one of the metals (blue and red bars), but many particles have a mixed core. By observing the histogram from the core to the surface, the two metals are increasingly mixed. Thus, the shell composition of most of the particles is 50% in each metal. These nanoparticles can be considered as an alloy. As the reduction rates of the two metals are more different (see Figure 1 from left to right) the structure starts to show an A-enriched core covered by a B-enriched shell (see Figure 1b, $v_A/v_B = 5$), until exhibiting a core-shell distribution in Figure 1c ($v_A/v_B = 10$): the core of most of the particles is formed by the faster metal (see red bars on the left), then the middle layers are slightly mixed, and the shell is mainly composed by the slower metal (see blue bars behind on the right). That is, a progressively better metal separation is obtained by increasing the reduction rate ratio [29].

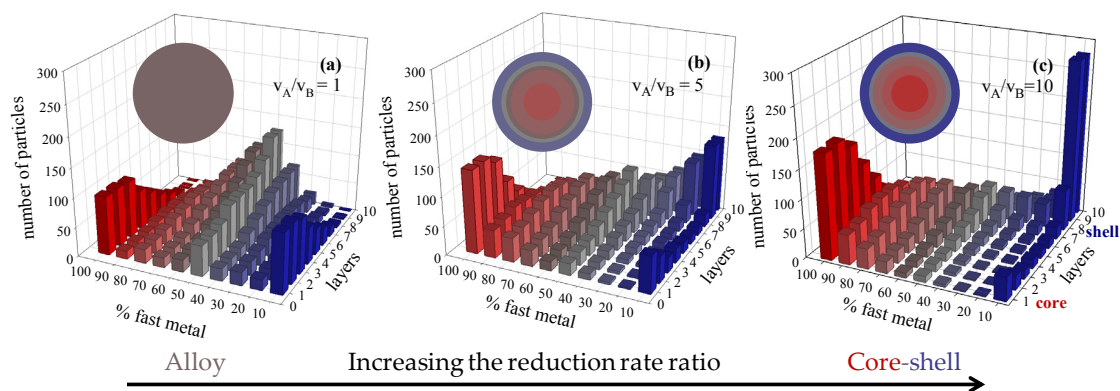


Figure 1. Histograms represent the number of particles with a given percentage of the faster reduction metal A in each layer, from the nanoparticle core to the surface, for different values of reduction rate ratio. (a) $v_A/v_B = 1$; (b) $v_A/v_B = 5$; and (c) $v_A/v_B = 10$. Synthesis conditions: flexible film ($k_{ex} = 5$, $f = 30$) and averaged metal salt concentration ($\langle c \rangle = 32$ metal salts in a micelle). Scheme color: blue (0%–45% of A), grey (45%–55% of A), and red (55%–100% of A). Less red means less A. Circles in each histogram represent nanoparticle structure in concentric layers, keeping the same color scheme. Data are taken from [100].

It is important to remark that each nanostructure is a reflection of the balance between the reduction rate of each metal precursor and the material intermicellar exchange rate. A more flexible surfactant film allows a faster material exchange [101] and, as a result, the difference between reduction rates is minimized, giving rise to a higher degree of mix [72]. This outcome can be clearly established from Table 1, by focusing our attention on nanoparticles prepared using a very flexible film, such as in a water/CTAB/isooctane/n-butanol microemulsion (see experiments number 15, 25, 28). All

particles are obtained as nanoalloys, in spite of the high differences in reduction potentials (Fe-Ni [74], $\Delta\varepsilon^0 = 0.20$ V; Pt-Cu [96], $\Delta\varepsilon^0 = 0.40$ V; Cu-Ni [76], $\Delta\varepsilon^0 = 0.58$ V). Note that the surfactants used in the experiments mentioned above (AOT and Brij-30) can be characterized as rigid ones, so the material intermicellar exchange is slow, in which case the difference in reduction rates cannot be attenuated.

3.2. Keeping the Pair of Metals Fixed

To make evident the effect of film flexibility on nanoparticle structure, one must pay attention to a particular pair of metals, and analyze how the metal segregation varies with the microemulsion composition. In the case of Pt-Ru (see experiments numbers 4–8), a nanoalloy was always obtained, both for rigid or flexible films. This can be explained on the basis of the very small difference in reduction rate ($\Delta\varepsilon^0 = 0.14$ V), which is not able to separate the metals, even with a slow intermicellar exchange rate. Effectively, if one observes the metal pairs with higher difference in reduction rate, the expected transition from a core-shell to a nanoalloy occurs as increasing flexibility is obtained. This is the case of Au-Ag, Au-Pt, and Au-Pd in Table 1. This result was also predicted by simulation [72], as shown in Figure 2. In this figure the difference in reduction potential is kept constant ($v_A/v_B = 10$), and the metal arrangements were obtained by employing different surfactant film flexibilities. The capacity of the microemulsion to minimize the difference between the reduction rates of the two metals is clearly reflected in the progressive mixture of the two metals as increasing the intermicellar exchange rate, which is mainly determined by the flexibility of the surfactant film.

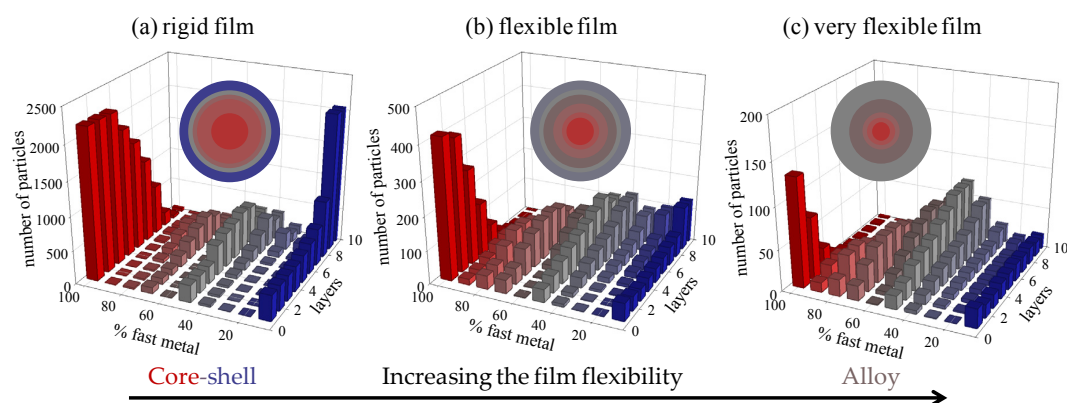


Figure 2. Number of particles versus the percentage of the faster reduction metal A in each layer, from the nanoparticle core to the surface, for different film flexibilities ((a) $k_{ex} = 1, f = 5$; (b) $k_{ex} = 5, f = 30$; and (c) $k_{ex} = 15, f = 90$), and keeping constant the reduction rate ratio ($v_A/v_B = 10$). Synthesis conditions: averaged metal salt concentration ($\langle c \rangle = 4$ metal salts in a micelle = 0.025 M). Scheme color: blue (0%–45% of A), grey (45%–55% of A), and red (55%–100% of A). Less red means less A. Circles in each histogram represent nanoparticle structures in concentric layers, maintaining the same color scheme. Adapted with permission from [72]. Copyright (2009) American Chemical Society.

It is interesting to point out that only alloys were obtained for $\Delta\varepsilon^0 < 0.20$ V (see Table 1, experiments 1–10). That is, it seems that a minimum difference in reduction rates $\Delta\varepsilon^0 \geq 0.20$ V is required to obtain a core-shell architecture, and this result cannot be modified by changing the microemulsion. Even using a rigid film (see experiments 1–4, 9), which implies a slow material exchange, experimental results show how a difference in reduction rates smaller than 0.20 V is not able to segregate the metals. This implies that if a core-shell structure is desired, but reduction rates are quite similar, or if the goal is to place the slower metal in the core, a one-pot method is ineffective and one must turn to a post-core method: first, one metal is reduced to form the core, then, the shell material is deposited on the first one by a second-step reduction.

Alternatively, it could be suggested that another option to obtain a segregated architecture could be a change in metal precursor. One must keep in mind that not just the final metal, but also the metal

precursor, influences the reduction rate, because the reduction potential of a metal is a characteristic feature of the concrete metal precursor. However, only the couple Pt-Pd (see experiments 9–11) has been obtained with different precursors. The reduction potentials of the Pd and Pt salts used in these experiments are shown as follows:

- Platinum salt $\text{H}_2[\text{PtCl}_6]$: This precursor was proved to be reduced from Pt^{4+} to Pt via Pt^{2+} [102] by means of the reactions: $\text{PtCl}_6^{2-} + 2\text{e}^- \rightarrow \text{PtCl}_4^{2-} + 2\text{Cl}^-$ ($\epsilon^0 = 0.726$ V [103]) and $\text{PtCl}_4^{2-} + 2\text{e}^- \rightarrow \text{Pt} + 2\text{Cl}^-$ ($\epsilon^0 = 0.758$ V [103]). From these data, standard electrode potential of the couple $\text{PtCl}_6^{2-}/\text{Pt}$ ($\text{PtCl}_6^{2-} + 4\text{e}^- \rightarrow \text{Pt} + 6\text{Cl}^-$) was calculated to be $\epsilon^0 = 0.742$ V [104]
- Platinum salt PtCl_2 : The standard electrode reduction is: $\text{Pt}^{2+} + 2\text{e}^- \rightarrow \text{Pt}$ ($\epsilon^0 = 1.188$ V [103])
- Palladium salt $\text{H}_2[\text{PdCl}_4]$: $\text{PdCl}_4^{2-} + 2\text{e}^- \rightarrow \text{Pd} + 2\text{Cl}^-$ ($\epsilon^0 = 0.591$ V [105])
- Palladium salt PdCl_2 : $\text{Pd}^{2+} + 2\text{e}^- \rightarrow \text{Pd}$ ($\epsilon^0 = 0.915$ V [103]).

Wu et al. [84] (experiment 9) used PtCl_6^{2-} and PdCl_4^{2-} salts as metal precursors, so $\Delta\epsilon^0 = 0.742 - 0.591 = 0.151$ V. Due to the small difference in reduction potential, an alloy was obtained in spite of the rigidity of the film (water/AOT/isooctane). An exhaustive study on the nanostructure of Pd-Pt nanoparticles by Chen et al. [106] leads to a similar result using the same metal salts and a water/AOT/n-heptane microemulsion (this experiment was not included in Table 1 because the mixing pattern was different). In experiment 10, Touroude et al. [85] used the same Pt precursor, but PdCl_2 as precursor, which gives Pd^{2+} ions, whose reduction potential is higher than PdCl_4^{2-} . Therefore, in the simultaneous reduction of Pd^{2+} and PtCl_6^{2-} the faster metal would be Pd, with a difference in standard potentials of $\Delta\epsilon^0 = 0.915 - 0.742 = 0.173$ V. Although the priority in reduction is inverted, there is only a slight difference between reduction potentials. This fact, added to the fast intermicellar exchange (flexible film), led to the true mixture of the metals. Finally, in experiment 11 [86], the metal salts were PdCl_2 and PtCl_2 , whose difference in standard potentials is higher: $\Delta\epsilon^0 = 1.188 - 0.915 = 0.273$ V. However, the salts (PdCl_2 and PtCl_2) were solved in dilute HCl solution [86], so the reactions $\text{PdCl}_2 + 2\text{HCl} \rightarrow \text{H}_2[\text{PdCl}_4]$ and $\text{PtCl}_4 + 2\text{HCl} \rightarrow \text{H}_2[\text{PtCl}_6]$ took place. Therefore, the ions inside micelles, before addition of the reducing agent, would be PdCl_4^{2-} and PtCl_6^{2-} , so the difference in reduction potentials would be smaller ($\Delta\epsilon^0 = 0.151$ V).

3.3. Changing Concentration

The tendency when increasing difference in reduction rates from an alloy to a core-shell is congruent until experiment number 24 (Pt-Cu pair). However, for the couples Pt-Cu, Pt-Bi, Cu-Ni, and Pt-Co, alloys were always obtained, in spite of the high difference in reduction rate. It could be understood on the basis of the very high flexibility of the microemulsion film (see experiments 25, 27, 28). However, even using a rigid film (experiments 24, 26, 29, 32) no experimental evidence of a segregated structure was obtained. The key parameter to understand these results is the metal salts concentration. It was proved both experimentally, and by simulation, that a minimum concentration is required to obtain a core-shell structure [75]. Figure 3 illustrates this behaviour. Au-Pt nanocatalyst was synthesized [75] using a one pot method in a 75% isooctane/20% tergitol/5% water microemulsion (flexible film). The Au-Pt nanoparticles were characterized using HR-STEM (High Resolution Scanning Transmission Electron Microscopy) and cross-sections scanned with EDX revealed their structure. The right column in Figure 3 shows the measured HR-STEM profiles of Au-Pt nanoparticles synthesized under different initial concentrations. All of the experimental conditions were reproduced by simulation for comparison purposes and theoretical STEM profiles were calculated from the structures predicted by simulation [75]. Left and center columns in Figure 3 show the histograms and theoretical STEM profiles ($\langle c[\text{AuCl}_4]^- \rangle = \langle c[\text{PtCl}_6]^{2-} \rangle = 2, 16, 32, 64$ atoms of precursors in a droplet, corresponding to 0.01, 0.08, 0.16, and 0.40 M). A reduction rate ratio $v_{\text{Au}}/v_{\text{Pt}} = 10$ was used to simulate the Au-Pt couple, and the isooctane/tergitol/water microemulsion was characterized by $f = 30$ and $k_{\text{ex}} = 5$ simulation parameters (see Supporting Information for Simulation Details). As expected, both experimental and simulated profiles show an enrichment in the slower reduction metal (Pt) in the

nanoparticle surface, whereas the core is mostly composed by Au, the metal which reduces faster. By observing the two types of profiles, one can conclude that the higher the concentration, the deeper the Pt profile. This means that the metal segregation is more pronounced as increasing concentration.

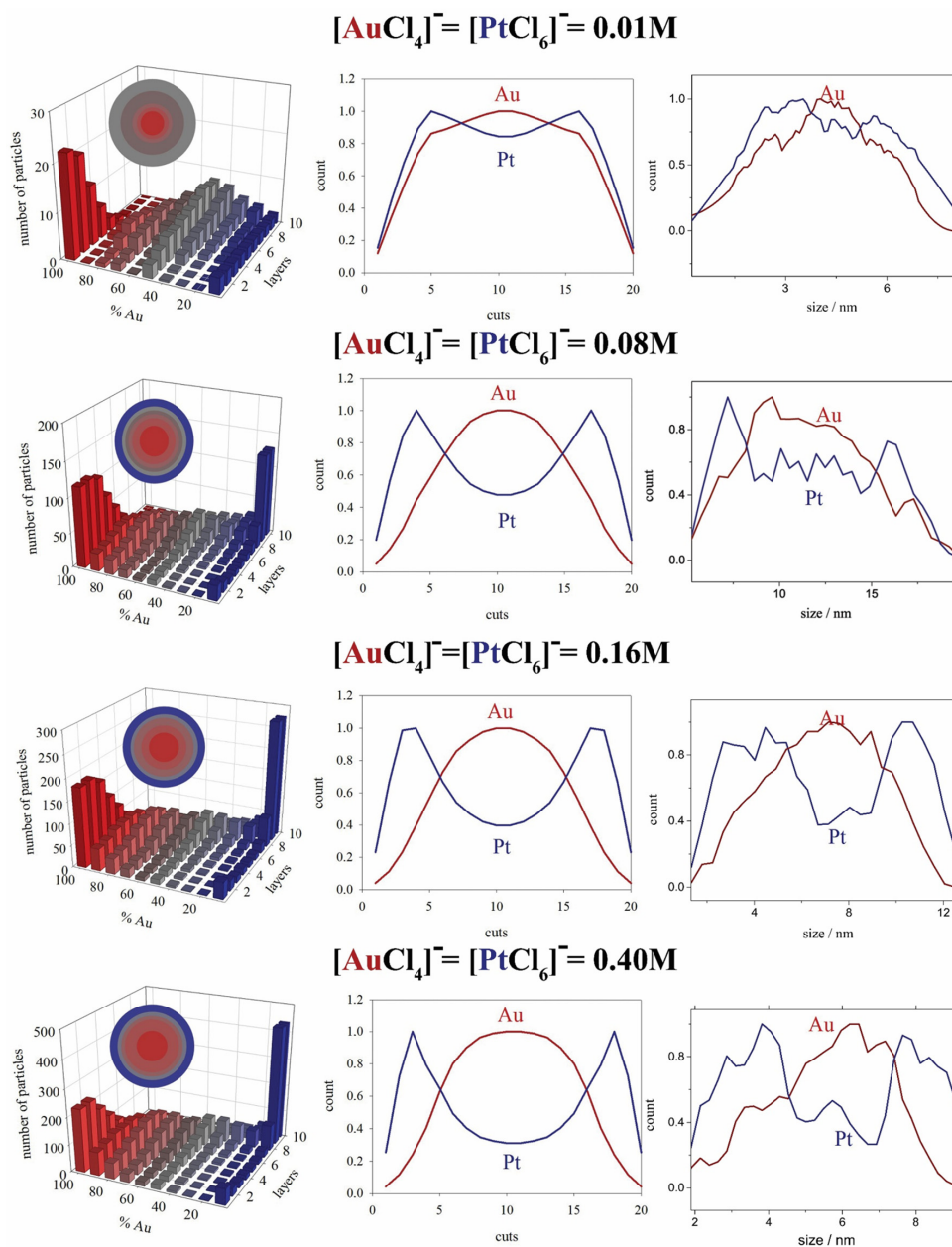


Figure 3. Left column: theoretical histograms for different concentrations (Au:Pt = 1:1). Colored spheres represent the average composition (red: Au, blue: Pt, grey: 50% Au-Pt). As the color turns to lighter tonalities, the proportion of pure metal in the layer is higher. Centre column: calculated STEM profiles for the average nanoparticle. Right column: measured STEM profiles for Au/Pt nanoparticles synthesized in a water/tergitol/isooctane microemulsion. Synthesis conditions: flexible film ($k_{ex} = 5$, $f = 30$); reduction rate ratio ($v_A/v_B = 10$). Adapted with permission from [75]. Copyright (2015) American Chemical Society.

The good agreement between experimental and simulation results supports the validity of the simulation model to predict the nanostructures. From this agreement, the model can be used to explain the role of concentration on metal arrangement in nanoparticles shown in Table 1: In Figure 3 one can

observe that a minimum concentration of 16 metal ions per micelle (0.08 M) is required to obtain a core-shell arrangement under this experimental condition (flexible film, $\Delta\epsilon^0 = 0.26$ V, $v_{\text{Au}}/v_{\text{Pt}} = 10$). Previous simulation results show that if the surfactant film was more rigid, a lower initial concentration (or 0.025 M) is enough to obtain metal separation (see Figure 1 in [107]). On the contrary, at high concentrations (0.40 M) a core-shell structure was always obtained even with very flexible films (see Figure 4 in [107]). In light of these results, structures in Table 1 can be reinterpreted according to concentrations: on the one hand, Au-Ag, Au-Pt, and Au-Pd nanoparticles can be obtained as core-shell not only if the film is rigid enough, but also if the metal ion concentration is high (at least 0.1 M for Au-Ag, 0.08 M for Au-Pt, and 0.5 M for Au-Pd, according to data reported in Table 1). On the other hand, although the concentration is increased, metal segregation is not possible when the difference in reduction rates is smaller than 0.20 V (see Pt-Ru and Pt-Pd nanoparticles). Finally, even when the difference in reduction rates was high, such as in experiments 23 to 29, a core-shell arrangement cannot be obtained at low concentration (note the quite low values of concentration in these experiments). In experiment 30, Ag-Ni nanocatalysts were obtained as a core-shell using a flexible film. Although the value of concentration is not available, the great value of nanoparticle size (50–100 nm) allows us to assume that a large metal ion concentration was used.

Finally, it can be advanced that the minimum concentration needed to get metal segregated nanocatalysts would be larger as the difference in reduction rates is larger [108]. From simulation results, and under the same synthesis conditions (flexible film), the concentration required to obtain a core-shell structure is a 0.025 M, 0.05 M, and 0.16 M when the reduction rates ratio are $v_{\text{A}}/v_{\text{B}} = 20$, 10, and 5, respectively [108].

4. Conclusions

The following conclusions can be drawn from this study:

1. A bimetallic nanocatalyst can be obtained as a nanoalloy or as a core-shell depending on the combination of metal precursors, microemulsion composition, and metal concentration;
2. A minimum difference is needed between the reduction standard potentials of the two metals of 0.20 V to obtain a core-shell structure. For values of $\Delta\epsilon^0$ smaller than 0.20 V the obtaining of alloy cannot be avoided, neither by changing the microemulsion nor by increasing the metal concentration;
3. As a rule, the higher the film flexibility around the micelles, the greater the degree of mixing in the nanocatalyst; and
4. A minimum concentration of metal precursors is required to obtain a core-shell structure. This minimum concentration depends on the microemulsion flexibility and on the difference in reduction rates.

Supplementary Materials: The following are available online at www.mdpi.com/2073-4344/7/2/68/s1: Simulation Model.

Acknowledgments: This work was supported by Axencia Galega de Innovación (Xunta de Galicia), MINECO, Spain (MAT2012-36754-C02-01), Xunta de Galicia, Spain (GRC2013-044, FEDER Funds). D.B. offers thanks the postdoc grant from Xunta de Galicia, Spain (POS-A/2013/018).

Author Contributions: M.A.L.Q. and C.T. conceived and designed the experiments; D.B. performed the experiments; M.A.L.Q. and C.T. and D.B. analyzed the data; C.T. wrote the paper.

Conflicts of Interest: The authors declare no conflict of interest.

References

1. Wang, W.; Vara, M.; Luo, M.; Huang, H.; Ruditskiy, A.; Park, J.; Bao, S.; Liu, J.; Howe, J.; Chi, M.; et al. Pd@Pt core-shell concave decahedra: A class of catalysts for the oxygen reduction reaction with enhanced activity and durability. *J. Am. Chem. Soc.* **2015**, *137*, 15036–15042. [[CrossRef](#)] [[PubMed](#)]

2. Yu, W.; Porosoff, M.D.; Chen, J.G. Review of Pt-based bimetallic catalysis: From model surfaces to supported catalysts. *Chem. Rev.* **2012**, *112*, 5780–5817. [[CrossRef](#)] [[PubMed](#)]
3. Ferrando, R.; Jellinek, J.; Johnston, R.L. Nanoalloys: From theory to applications of alloy clusters and nanoparticles. *Chem. Rev.* **2008**, *108*, 845–910. [[CrossRef](#)] [[PubMed](#)]
4. Yuan, P.; Ma, R.; Gao, N.; Garai, M.; Xu, Q.-H. Plasmon coupling-enhanced two-photon photoluminescence of Au@Ag core-shell nanoparticles and applications in the nuclease assay. *Nanoscale Res. Lett.* **2015**, *7*, 10233–10239. [[CrossRef](#)] [[PubMed](#)]
5. Gao, M.-R.; Xu, Y.-F.; Jiang, J.; Yu, S.-H. Nanostructured metal chalcogenides: Synthesis, modification, and applications in energy conversion and storage devices. *Chem. Soc. Rev.* **2013**, *42*, 2986–3017. [[CrossRef](#)]
6. Tuae, X.; Rudi, S.; Petkov, V.; Hoell, A.; Strasser, P. In situ study of atomic structure transformations of Pt-Ni nanoparticle catalysts during electrochemical potential cycling. *ACS Nano* **2013**, *7*, 5666–5674. [[CrossRef](#)] [[PubMed](#)]
7. Gu, X.; Lu, Z.-H.; Jiang, H.-L.; Akita, T.; Xu, Q. Synergistic catalysis of metal-organic framework-immobilized Au-Pd nanoparticles in dehydrogenation of formic acid for chemical hydrogen storage. *J. Am. Chem. Soc.* **2011**, *133*, 11822–11825. [[CrossRef](#)] [[PubMed](#)]
8. Liang, M.; Wang, L.; Su, R.; Qi, W.; Wang, M.; Yu, Y.; He, Z. Synthesis of silver nanoparticles within cross-linked lysozyme crystals as recyclable catalysts for 4-nitrophenol reduction. *Catal. Sci. Technol.* **2013**, *3*, 1910–1914. [[CrossRef](#)]
9. Panacek, A.; Prucek, R.; Hrbac, J.; Nevecna, T.; Steffkova, J.; Zboril, R.; Kvitek, L. Polyacrylate-assisted size control of silver nanoparticles and their catalytic activity. *Chem. Mat.* **2014**, *26*, 1332–1339. [[CrossRef](#)]
10. Sinfelt, J.H. Catalysis by alloys and bimetallic clusters. *Acc. Chem. Res.* **1977**, *10*, 15–20. [[CrossRef](#)]
11. Sinfelt, J.H. Structure of bimetallic clusters. *Acc. Chem. Res.* **1987**, *20*, 134–139. [[CrossRef](#)]
12. Tedsree, K.; Li, T.; Jones, S.; Chan, C.W.A.; Yu, K.M.K.; Bagot, P.A.J.; Marquis, E.A.; Smith, G.D.W.; Tsang, S.C.E. Hydrogen production from formic acid decomposition at room temperature using a Ag-Pd core-shell nanocatalyst. *Nat. Nanotechnol.* **2011**, *6*, 302–307. [[CrossRef](#)] [[PubMed](#)]
13. Bandarenka, A.S.; Varela, A.S.; Karamad, M.; Calle-Vallejo, F.; Bech, L.; Perez-Alonso, F.J.; Rossmeisl, J.; Stephens, I.E.L.; Chorkendorff, I. Design of an active site towards optimal electrocatalysis: Overlayers, surface alloys and near-surface alloys of Cu/Pt(111). *Angew. Chem. Int. Ed.* **2012**, *51*, 11845–11848. [[CrossRef](#)] [[PubMed](#)]
14. Spanos, I.; Dideriksen, K.; Kirkensgaard, J.J.K.; Jelavic, S.; Arenz, M. Structural disordering of de-alloyed Pt bimetallic nanocatalysts: The effect on oxygen reduction reaction activity and stability. *Phys. Chem. Chem. Phys.* **2015**, *17*, 28044–28053. [[CrossRef](#)] [[PubMed](#)]
15. König, R.Y.G.; Schwarze, M.; Schomäcker, R.; Stubenrauch, C. Catalytic Activity of Mono- and Bi-Metallic Nanoparticles Synthesized via Microemulsions. *Catalysts* **2014**, *4*, 256–275. [[CrossRef](#)]
16. Singh, H.P.; Gupta, N.; Sharma, S.K.; Sharma, R.K. Synthesis of bimetallic Pt-Cu nanoparticles and their application in the reduction of rhodamine B. *Colloids Surf. A* **2013**, *416*, 43–50. [[CrossRef](#)]
17. Zielinska-Jurek, A.; Kowalska, E.; Sobczak, J.W.; Lisowski, W.; Ohtani, B.; Zaleska, A. Preparation and characterization of monometallic (Au) and bimetallic (Ag/Au) modified-titania photocatalysts activated by visible light. *Appl. Catal. B* **2011**, *101*, 504–514. [[CrossRef](#)]
18. Santhanalakshmi, J.; Venkatesan, P. Mono and bimetallic nanoparticles of gold, silver and palladium-catalyzed NADH oxidation-coupled reduction of Eosin-Y. *J. Nanoparticle Res.* **2011**, *13*, 479–490. [[CrossRef](#)]
19. Heshmatpour, F.; Abazari, R.; Balalaie, S. Preparation of monometallic (Pd, Ag) and bimetallic (Pd/Ag, Pd/Ni, Pd/Cu) nanoparticles via reversed micelles and their use in the Heck reaction. *Tetrahedron* **2012**, *68*, 3001–3011. [[CrossRef](#)]
20. Notar Francesco, I.; Fontaine-Vive, F.; Antoniotti, S. Synergy in the catalytic activity of bimetallic nanoparticles and new synthetic methods for the preparation of fine chemicals. *Chem. Cat. Chem.* **2014**, *6*, 2784–2791. [[CrossRef](#)]
21. Jiang, H.-L.; Xu, Q. Recent progress in synergistic catalysis over heterometallic nanoparticles. *J. Mater. Chem.* **2011**, *21*, 13705–13725. [[CrossRef](#)]
22. Hernández-Fernández, P.; Rojas, S.; Ocón, P.; Gómez de la Fuente, J.L.; San Fabián, J.; Sanza, J.; Peña, M.A.; García-García, F.J.; Terreros, P.; Fierro, J.L.G. Influence of the preparation route of bimetallic Pt-Au

- nanoparticle electrocatalyst for the oxygen reduction reaction. *J. Phys. Chem. B* **2007**, *111*, 2913–2923. [[CrossRef](#)]
23. Boutonnet, M.; Lögdberg, S.; Svensson, E.E. Recent developments in the application of nanoparticles prepared from w/o microemulsions in heterogeneous catalysis. *Curr. Opin. Colloid Interface Sci.* **2008**, *13*, 270–286. [[CrossRef](#)]
 24. Wen, M.; Mori, K.; Kuwahara, Y.; Yamashita, H. Plasmonic Au@Pd nanoparticles supported on a basic metal-organic framework: Synergic boosting of H₂ production from formic acid. *ACS Energy Lett.* **2017**, *2*, 1–7. [[CrossRef](#)]
 25. Wang, A.-Q.; Chang, C.-M.; Mou, C.-Y. Evolution of catalytic activity of Au-Ag bimetallic nanoparticles on mesoporous support for CO oxidation. *J. Phys. Chem. B* **2005**, *109*, 18860–18867. [[CrossRef](#)] [[PubMed](#)]
 26. Shi, J. On the synergetic catalytic effect in heterogeneous nanocomposite catalysts. *Chem. Rev.* **2013**, *113*, 2139–2181. [[CrossRef](#)] [[PubMed](#)]
 27. Navarro, R.M.; Pawelec, B.; Trejo, J.M.; Mariscal, R.; Fierro, J.L.G. Hydrogenation of aromatics on sulfur-resistant PtPd bimetallic catalysts. *J. Catal.* **2000**, *189*, 184–194. [[CrossRef](#)]
 28. Hermans, S.; Raja, R.; Thomas, J.M.; Johnson, B.F.G.; Sankar, G.; Gleeson, D. Solvent-free, low-temperature, selective hydrogenation of polyenes using a bimetallic nanoparticle Ru-Sn catalyst. *Angew. Chem. Int. Ed.* **2001**, *40*, 1211–1215. [[CrossRef](#)]
 29. Lu, P.; Teranishi, T.; Asakura, K.; Miyake, M.; Toshima, N. Polymer-protected Ni/Pd bimetallic nano-clusters: Preparation, characterization and catalysis for hydrogenation of nitrobenzene. *J. Phys. Chem. B* **1999**, *103*, 9673–9682. [[CrossRef](#)]
 30. Cheney, B.A.; Lauterbach, J.A.; Chen, J.G. Reverse micelle synthesis and characterization of supported Pt/Ni bimetallic catalysts on γ -Al₂O₃. *App. Catal. A* **2011**, *394*, 41–47. [[CrossRef](#)]
 31. Parera, J.M.; Beltramini, J.N. Stability of bimetallic reforming catalysts. *J. Catal.* **1988**, *112*, 357–365. [[CrossRef](#)]
 32. Skoplyak, O.; Menning, C.A.; Barteau, M.A.; Chen, J.G. Reforming of oxygenates for H₂ production on 3d/Pt(111) bimetallic surfaces. *Top. Catal.* **2008**, *51*, 49–59. [[CrossRef](#)]
 33. Peng, X.; Pan, Q.; Rempel, G.L. Bimetallic dendrimer-encapsulated nanoparticles as catalysts: A review of the research advances. *Chem. Soc. Rev.* **2008**, *37*, 1619–1628. [[CrossRef](#)] [[PubMed](#)]
 34. Murahashi, S.; Naota, T.; Hirai, N. Aerobic oxidation of alcohols with ruthenium-cobalt bimetallic catalyst in the presence of aldehydes. *J. Org. Chem.* **1993**, *58*, 7318–7319. [[CrossRef](#)]
 35. Araña, J.; Ramírez de la Piscina, P.; Llorca, J.; Sales, J.; Homs, N.; Fierro, J.L.G. Bimetallic silica-supported catalysts based on Ni-Sn, Pd-Sn, and Pt-Sn as materials in the CO oxidation reaction. *Chem. Mater.* **1998**, *10*, 1333–1342. [[CrossRef](#)]
 36. Dhakad, M.; Fino, D.; Rayalu, S.; Kumar, R.; Watanabe, A.; Haneda, H.; Devotta, S.; Mitsunashi, T.; Labhsetwar, N. Zirconia supported Ru-Co bimetallic catalysts for diesel soot oxidation. *Top. Catal.* **2007**, *42*, 273–276. [[CrossRef](#)]
 37. Zhao, L.; Thomas, J.P.; Heinig, N.F.; Abd-Ellah, M.; Wang, X.; Leung, K.T. Au-Pt alloy nanocatalysts for electro-oxidation of methanol and their application for fast-response non-enzymatic alcohol sensing. *J. Mater. Chem. C* **2014**, *2*, 2707–2714. [[CrossRef](#)]
 38. Shao, M.; Peles, A.; Shoemaker, K.; Gummalla, M.; Njoki, P.N.; Luo, J.; Zhong, C.-J. Enhanced oxygen reduction activity of platinum monolayer on gold nanoparticles. *J. Phys. Chem. Lett.* **2011**, *2*, 67–72. [[CrossRef](#)] [[PubMed](#)]
 39. Wang, D.; Yu, Y.; Xin, H.L.; Hovden, R.; Ercius, P.; Mundy, J.A.; Chen, H.; Richard, J.H.; Muller, D.A.; DiSalvo, F.J.; et al. Tuning oxygen reduction reaction activity via controllable dealloying: A model study of ordered Cu₃Pt/C intermetallic nanocatalysts. *Nano Lett.* **2012**, *12*, 5230–5238. [[CrossRef](#)] [[PubMed](#)]
 40. Koh, S.; Strasser, P. Electrocatalysis on bimetallic surfaces: Modifying catalytic reactivity for oxygen reduction by voltammetric surface dealloying. *J. Am. Chem. Soc.* **2007**, *129*, 12624–12625. [[CrossRef](#)] [[PubMed](#)]
 41. Gan, L.; Heggen, M.; Rudi, S.; Strasser, P. Core-shell compositional fine structures of dealloyed Pt_xNi_{1-x} nanoparticles and their impact on oxygen reduction catalysis. *Nano Lett.* **2012**, *12*, 5423–5430. [[CrossRef](#)] [[PubMed](#)]
 42. Ruppert, A.M.; Weinberg, K.; Palkovits, R. Hydrogenolysis goes bio: From carbohydrates and sugar alcohols to platform chemicals. *Angew. Chem. Int. Ed.* **2012**, *51*, 2564–2601. [[CrossRef](#)] [[PubMed](#)]

43. Ichikawa, M.; Rao, L.; Ito, T.; Fukuoka, A. Ensemble and ligand effects in selective alkane hydrogenolysis catalyzed on well characterized rhodium-iridium and rhodium-iron bimetallic clusters inside NaY zeolite. *Faraday Discuss. Chem. Soc. Rev.* **1989**, *87*, 321–336.
44. Zhou, S.; Johnson, M.; Veinot, J.G.C. Iron/iron oxide nanoparticles: A versatile support for catalytic metals and their application in Suzuki-Miyaura cross-coupling reactions. *Chem. Commun.* **2010**, *46*, 2411–2413. [[CrossRef](#)]
45. Hudson, R.; Li, C.-J.; Moores, A. Magnetic copper-iron nanoparticles as simple heterogeneous catalysts for the azide-alkyne click reaction in water. *Green Chem.* **2012**, *14*, 622–624. [[CrossRef](#)]
46. Rai, R.K.; Tyagi, D.; Gupta, K.; Singh, S.K. Activated nanostructured bimetallic catalysts for C-C coupling reactions: Recent progress. *Catal. Sci. Technol.* **2016**, *6*, 3341–3361. [[CrossRef](#)]
47. Sankar, M.; Dimitratos, N.; Miedziak, P.J.; Wells, P.P.; Kiely, C.J.; Hutchings, G.J. Designing bimetallic catalysts for a green and sustainable future. *Chem. Soc. Rev.* **2012**, *41*, 8099–8139. [[CrossRef](#)] [[PubMed](#)]
48. Bracey, C.L.; Ellis, P.R.; Hutchings, G.J. Application of copper-gold alloys in catalysis: Current status and future perspectives. *Chem. Soc. Rev.* **2009**, *38*, 2231–2243. [[CrossRef](#)] [[PubMed](#)]
49. Toshima, N.; Yonezawa, T. Bimetallic nanoparticles—Novel materials for chemical and physical applications. *New J. Chem.* **1998**, *22*, 1179–1201. [[CrossRef](#)]
50. Bönnemann, H.; Richards, R.M. Nanoscopic metal particles—Synthetic methods and potential applications. *Eur. J. Inorg. Chem.* **2001**, *2001*, 2455–2480. [[CrossRef](#)]
51. Muñoz-Flores, B.M.; Kharisov, B.I.; Jiménez-Pérez, V.M.; Elizondo Martínez, P.; López, S.T. Recent advances in the synthesis and main applications of metallic nanoalloys. *Ind. Eng. Chem. Res.* **2011**, *50*, 7705–7721. [[CrossRef](#)]
52. Suntivich, J.; Xu, Z.; Carlton, C.E.; Kim, J.; Han, B.; Lee, S.W.; Bonnet, N.; Marzari, N.; Allard, L.F.; Gasteiger, H.A.; et al. Surface composition tuning of Au-Pt bimetallic nanoparticles for enhanced carbon monoxide and methanol electro-oxidation. *J. Am. Chem. Soc.* **2013**, *135*, 7985–7991. [[CrossRef](#)] [[PubMed](#)]
53. Hwang, B.J.; Sarma, L.S.; Chen, J.M.; Chen, C.H.; Shih, S.C.; Wang, G.R.; Liu, D.G.; Lee, J.F.; Tang, M.T. Structural models and atomic distribution of bimetallic nanoparticles as investigated by X-ray Absorption spectroscopy. *J. Am. Chem. Soc.* **2005**, *127*, 11140–11145. [[CrossRef](#)] [[PubMed](#)]
54. Somorjai, G.A.; Park, J.Y. Molecular factors of catalytic selectivity. *Angew. Chem. Int. Ed.* **2008**, *47*, 9212–9228. [[CrossRef](#)] [[PubMed](#)]
55. Liao, H.; Fisher, A.; Xu, Z.J. Surface segregation in bimetallic nanoparticles: A critical issue in electrocatalyst engineering. *Small* **2015**, *11*, 3221–3246. [[CrossRef](#)] [[PubMed](#)]
56. Hartl, K.; Mayrhofer, K.J.J.; López, M.; Goia, D.; Arenz, M. AuPt core-shell nanocatalysts with bulk Pt activity. *Electrochem. Commun.* **2010**, *12*, 1487–1489. [[CrossRef](#)]
57. Zhang, G.-R.; Zhao, D.; Feng, Y.-Y.; Zhang, B.; Su, D.S.; Liu, G.; Xu, B.-Q. Catalytic Pt-on-Au nanostructures: Why Pt becomes more active on smaller Au particles. *ACS Nano* **2012**, *6*, 2226–2236. [[CrossRef](#)] [[PubMed](#)]
58. Feng, L.; Gao, G.; Huang, P.; Wang, K.; Wang, X.; Luo, T.; Zhang, C. Optical properties and catalytic activity of bimetallic gold-silver nanoparticles. *Nano Biomed. Eng.* **2010**, *2*, 258–267. [[CrossRef](#)]
59. Chen, G.; Desinan, S.; Nechache, R.; Rosei, R.; Rosei, F.; Ma, D. Bifunctional catalytic/magnetic Ni@Ru core-shell nanoparticles. *Chem. Commun.* **2011**, *47*, 6308–6310. [[CrossRef](#)] [[PubMed](#)]
60. Magno, L.M.; Sigle, W.; Aken, P.A.v.; Angelescu, D.G.; Stubenrauch, C. Microemulsions as reaction media for the synthesis of bimetallic nanoparticles: Size and composition of particles. *Chem. Mater.* **2010**, *22*, 6263–6271. [[CrossRef](#)]
61. Xu, Z.; Hou, Y.; Sun, S. Magnetic core/shell Fe₃O₄/Au and Fe₃O₄/Au/Ag nanoparticles with tunable plasmonic properties. *J. Am. Chem. Soc.* **2007**, *129*, 8698. [[CrossRef](#)] [[PubMed](#)]
62. Zubris, M.; King, R.B.; Garmestani, H.; Tannenbaum, R. FeCo nanoalloy formation by decomposition of their carbonyl precursors. *J. Mater. Chem.* **2005**, *15*, 1277–1285. [[CrossRef](#)]
63. Kolb, U.; Quaiser, S.A.; Winter, M.; Reetz, M.T. Investigation of tetraalkylammonium bromide stabilized palladium/platinum bimetallic clusters using extended X-ray absorption fine structure spectroscopy. *Chem. Mater.* **1996**, *8*, 1889–1894. [[CrossRef](#)]
64. Juškėnas, R.; Mockus, Z.; Kanapekaitė, S.; Stalnionis, G.; Survila, A. XRD studies of the phase composition of the electrodeposited copper-rich Cu–Sn alloys. *Electrochim. Acta* **2006**, *52*, 928–935.
65. Abdelsayed, V.; Aljarash, A.; El-Shall, M.S.; Othman, Z.A.; Alghamdi, A.H. Microwave synthesis of bimetallic nanoalloys and CO oxidation on ceria-supported nanoalloys. *Chem. Mater.* **2009**, *21*, 2825–2834. [[CrossRef](#)]

66. Gerbec, J.A.; Magana, D.; Washington, A.; Strouse, G.F. Microwave-enhanced reaction rates for nanoparticle synthesis. *J. Am. Chem. Soc.* **2005**, *127*, 15791–15800. [[CrossRef](#)] [[PubMed](#)]
67. Feng, J.; Zhang, C. Preparation of Cu-Ni alloy nanocrystallites in water-in-oil microemulsions. *J. Colloid Interface Sci.* **2006**, *293*, 414–420. [[CrossRef](#)] [[PubMed](#)]
68. Yin, Z.; Ma, D.; Bao, X. Emulsion-assisted synthesis of monodisperse binary metal nanoparticles. *Chem. Commun.* **2010**, *46*, 1344–1346. [[CrossRef](#)] [[PubMed](#)]
69. Parapat, R.Y.; Parwoto, V.; Schwarze, M.; Zhang, B.; Su, D.-S.; Schomäcker, R. A new method to synthesize very active and stable supported metal Pt catalysts: Thermo-destabilization of microemulsions. *J. Mater. Chem.* **2012**, *22*, 11605–11614. [[CrossRef](#)]
70. Chen, Y.; Wang, W.G.; Zhou, S. Size effect of Au seeds on structure of Au-Pt bimetallic nanoparticles. *Mater. Lett.* **2011**, *65*, 2649–2651. [[CrossRef](#)]
71. Fletcher, P.D.I.; Howe, A.M.; Robinson, B.H. The kinetics of solubilise exchange between water droplets of a water-in-oil microemulsion. *J. Chem. Soc. Faraday Trans.* **1987**, *83*, 985–1006. [[CrossRef](#)]
72. Tojo, C.; de Dios, M.; López-Quintela, M.A. On the structure of bimetallic nanoparticles synthesized in microemulsions. *J. Phys. Chem. C* **2009**, *113*, 19145–19154. [[CrossRef](#)]
73. López-Quintela, M.A. Synthesis of nanomaterials in microemulsions: Formation mechanisms and growth control. *Curr. Opin. Colloid Interface. Sci.* **2003**, *8*, 137–144. [[CrossRef](#)]
74. Ban, I.; Drofenik, M.; Makovec, D. The synthesis of iron-nickel alloy nanoparticles using a reverse micelle technique. *J. Magn. Magn. Mater.* **2006**, *307*, 250–256. [[CrossRef](#)]
75. Buceta, D.; Tojo, C.; Vukmirovik, M.; Deepak, F.L.; López-Quintela, M.A. Controlling bimetallic nanostructures by the microemulsion method with sub-nanometer resolution using a prediction model. *Langmuir* **2015**, *31*, 7435–7439. [[CrossRef](#)] [[PubMed](#)]
76. Ahmed, J.; Ramanujachary, K.V.; Lofland, S.E.; Furiato, A.; Gupta, G.; Shivaprasad, S.M.; Ganguli, A.K. Bimetallic Cu-Ni nanoparticles of varying composition (CuNi₃, CuNi, Cu₃Ni). *Colloids Surf. A* **2008**, *331*, 206–212. [[CrossRef](#)]
77. Wu, M.; Lai, L. Synthesis of Pt/Ag bimetallic nanoparticles in water-in-oil microemulsions. *Colloids Surf. A* **2004**, *244*, 149–157. [[CrossRef](#)]
78. Wei, G.; Dai, W.; Qian, L.; Cao, W.; Zhang, J. Reverse microemulsions synthesis and characterization of Pd-Ag bimetallic alloy catalysts supported on Al₂O₃ for acetylene hydrogenation. *China Pet. Process. Petrochem. Technol.* **2012**, *14*, 59–67.
79. Solla-Gullón, J.; Vidal-Iglesias, F.J.; Montiel, V.; Aldaz, A. Electrochemical characterization of platinum-ruthenium nanoparticles prepared by water-in-oil microemulsion. *Electrochim. Acta* **2004**, *49*, 5079–5088. [[CrossRef](#)]
80. Rojas, S.; García-García, F.J.; Jaeras, S.; Martínez-Huerta, M.V.; García Fierro, J.L.; Boutonnet, M. Preparation of carbon supported Pt and PtRu nanoparticles from microemulsion. *Appl. Catal. A* **2005**, *285*, 24–35. [[CrossRef](#)]
81. Liu, Z.; Lee, J.Y.; Han, M.; Chen, W.; Gan, L.M. Synthesis and characterization of PtRu/C catalysts from microemulsions and emulsions. *J. Mater. Chem.* **2002**, *12*, 2453–2458. [[CrossRef](#)]
82. Kim, T.; Koboyashi, K.; Nagai, M. Preparation and characterization of platinum-ruthenium bimetallic nanoparticles using reverse microemulsions for fuel cell catalyst. *J. Oleo Sci.* **2007**, *56*, 553–562. [[CrossRef](#)] [[PubMed](#)]
83. Zhang, X.; Chan, K.Y. Water-in-oil microemulsion synthesis of platinum-ruthenium nanoparticles, their characterization and electrocatalytic properties. *Chem. Mater.* **2003**, *15*, 451–459. [[CrossRef](#)]
84. Wu, M.; Chen, D.; Huang, T. Preparation of Pd/Pt bimetallic nanoparticles in water/AOT/isooctane microemulsions. *J. Colloids Interface Sci.* **2001**, *243*, 102–108. [[CrossRef](#)]
85. Touroude, R.; Girard, P.; Maire, G.; Kizling, J.; Boutonnet, M.; Stenius, P. Preparation of colloidal platinum/palladium alloy particles from non-ionic microemulsions: Characterization and catalytic behaviour. *Colloids Surf. A* **1992**, *67*, 9–19. [[CrossRef](#)]
86. Yashima, M.; Falk, L.K.L.; Palmqvist, A.E.C.; Holmberg, K. Structure and catalytic properties of nanosized alumina supported platinum and palladium particles synthesized by reaction in microemulsion. *J. Colloids Interface Sci.* **2003**, *268*, 348–356. [[CrossRef](#)]
87. Chen, D.; Chen, C. Formation and characterization of Au-Ag bimetallic nanoparticles in water-in-oil microemulsions. *J. Mater. Chem.* **2002**, *12*, 1557–1562. [[CrossRef](#)]

88. Cheng, J.; Bordes, R.; Olsson, E.; Holmberg, K. One-pot synthesis of porous gold nanoparticles by preparation of Ag/Au nanoparticles followed by dealloying. *Colloids Surf. A* **2013**, *436*, 823–829. [[CrossRef](#)]
89. Pal, A.; Shah, S.; Devi, S. Preparation of silver, gold and silver-gold bimetallic nanoparticles in w/o microemulsion containing Triton X-100. *Colloids Surf. A* **2007**, *302*, 483–487. [[CrossRef](#)]
90. Wu, M.; Chen, D.; Huang, T. Preparation of Au/Pt bimetallic nanoparticles in water-in-oil microemulsions. *Chem. Mater.* **2001**, *13*, 599–606. [[CrossRef](#)]
91. Habrioux, A.; Vogel, W.; Guinel, M.; Guetaz, L.; Servat, K.; Kokoh, B.; Alonso-Vante, N. Structural and electrochemical studies of Au-Pt nanoalloys. *Phys. Chem. Chem. Phys.* **2009**, *11*, 3573–3579. [[CrossRef](#)] [[PubMed](#)]
92. Pal, A. Gold–platinum alloy nanoparticles through water-in-oil microemulsion. *J. Nanostruct. Chem.* **2015**, *5*, 65–69. [[CrossRef](#)]
93. Wu, M.; Chen, D.; Huang, T. Synthesis of Au/Pd bimetallic nanoparticles in reverse micelles. *Langmuir* **2001**, *17*, 3877–3883. [[CrossRef](#)]
94. Simoes, M.; Baranton, S.; Coutanceau, C. Electrooxidation of sodium borohydride at Pd, Au, and Pd_xAu_{1-x} carbon-supported nanocatalysts. *J. Phys. Chem. C* **2009**, *113*, 13369–13376. [[CrossRef](#)]
95. Li, T.; Zhou, H.; Huang, J.; Yin, J.; Chen, Z.; Liu, D.; Zhang, N.; Kuang, Y. Facile preparation of Pd-Au bimetallic nanoparticles via in-situ self-assembly in reverse microemulsion and their electrocatalytic properties. *Colloids Surf. A* **2014**, *463*, 55–62. [[CrossRef](#)]
96. Weihua, W.; Xuelin, T.; Kai, C.; Gengyu, C. Synthesis and characterization of Pt-Cu bimetallic alloy nanoparticles by reverse micelles method. *Colloids Surf. A* **2006**, *273*, 35. [[CrossRef](#)]
97. Zhang, X.; Chan, K.Y. Microemulsion synthesis and electrocatalytic properties of Platinum-Cobalt nanoparticles. *J. Mater. Chem.* **2002**, *12*, 1203–1206. [[CrossRef](#)]
98. Xia, L.; Hu, X.; Kang, X.; Zhao, H.; Sun, M.; Cihen, X. A one-step facile synthesis of Ag-Ni core-shell nanoparticles in water-in-oil microemulsions. *Colloids Surf. A* **2010**, *367*, 96–101. [[CrossRef](#)]
99. Heshmatpour, F.; Abazari, R. Formation of dispersed palladium-nickel bimetallic nanoparticles in microemulsions: Synthesis, characterization, and their use as efficient heterogeneous recyclable catalysts for the amination reactions of aryl chlorides under mild conditions. *RSC Adv.* **2014**, *4*, 55815–55826. [[CrossRef](#)]
100. Tojo, C.; Vila-Romeu, N. Kinetic study on the formation of bimetallic core-shell nanoparticles via microemulsions. *Materials* **2014**, *7*, 7513–7532. [[CrossRef](#)]
101. López-Quintela, M.A.; Tojo, C.; Blanco, M.C.; García Río, L.; Leis, J.R. Microemulsion dynamics and reactions in microemulsions. *Curr. Opin. Colloid Interface Sci.* **2004**, *9*, 264–279. [[CrossRef](#)]
102. Hwang, B.-J.; Tsai, Y.-W.; Sarma, L.S.; Tseng, Y.-L.; Liu, D.-G.; Lee, J.-F. Genesis of bimetallic Pt-Cu clusters in reverse micelles investigated by in situ X-ray absorption spectroscopy. *J. Phys. Chem. B* **2004**, *108*, 20427–20434. [[CrossRef](#)]
103. Bard, A.J.; Faulkner, L.R. Electrochemical methods. In *Fundamentals and Applications*, 2nd ed.; John Wiley and Sons Inc.: New York, NY, USA, 2001.
104. Li, Y.; Jiang, Y.; Chen, M.; Liao, H.; Huang, R.; Zhou, Z.; Tian, N.; Chen, S.; Sun, S. Electrochemically shape-controlled synthesis of trapezohedral platinum nanocrystals with high electrocatalytic activity. *Chem. Commun.* **2012**, *48*, 9531–9533. [[CrossRef](#)] [[PubMed](#)]
105. Liu, G.; Eichelsdoerfer, D.J.; Rasin, B.; Zhou, Y.; Brown, K.A.; Liao, X.; Mirkin, C.A. Delineating the pathways for the site-directed synthesis of individual nanoparticles on surfaces. *Proc. Natl. Acad. Sci. USA* **2013**, *110*, 887–891. [[CrossRef](#)] [[PubMed](#)]
106. Chen, C.; Hwang, B.; Wang, G.; Subramanya Sarma, L.; Tang, M.; Liu, D.; Lee, J. Nucleation and Growth Mechanism of Pd/Pt Bimetallic Clusters in Sodium Bis(2-ethylhexyl) sulfosuccinate (AOT) Reverse Micelles as Studied by in Situ X-ray Absorption Spectroscopy. *J. Phys. Chem. B* **2005**, *109*, 21566–21575. [[CrossRef](#)] [[PubMed](#)]
107. Tojo, C.; Buceta, D.; López-Quintela, M.A. Understanding the Metal Distribution in Core-Shell Nanoparticles Prepared in Micellar Media. *Nanoscale Res. Lett.* **2015**, *10*, 339–349. [[CrossRef](#)] [[PubMed](#)]
108. Tojo, C.; Buceta, D.; López-Quintela, M.A. A kinetic study on simultaneous reduction of metals within reverse micelles. **2017**, to be published.

